

Figure S1

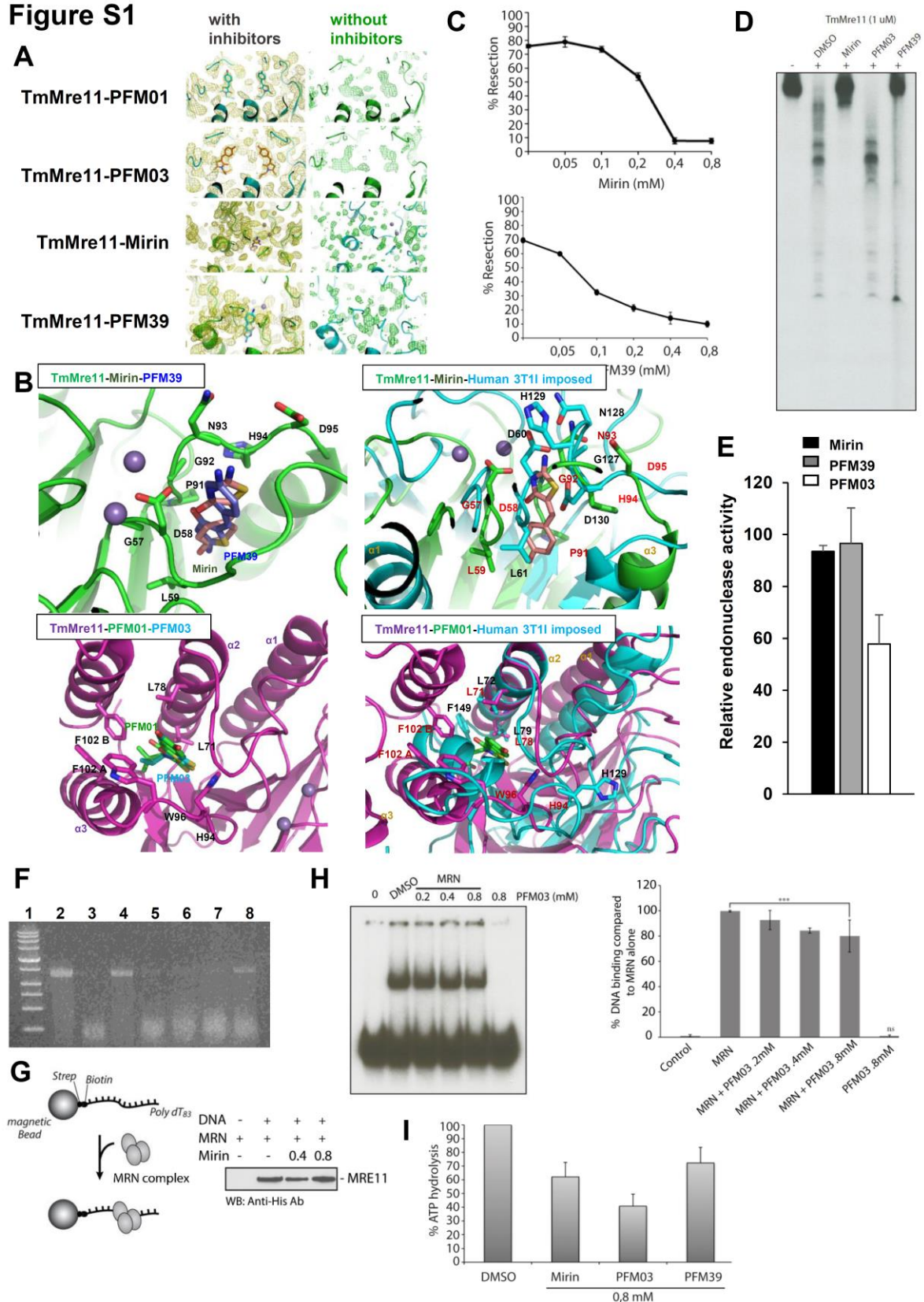


Figure S1, related to Figure 1, provides further details of the structural analysis of MRE11 inhibitors and their biochemical characterisation.

Legend to Figure S1.

(A) Electron density maps for the inhibitor structures and TmMre11. The left hand panels show Fo-Fc maps contoured at 1.0 sigma with the inhibitors in place. The right hand panels are 2Fo-Fc maps at 2.0 sigma without the inhibitors in place. Sequence alignment of TmMre11 and hMRE11 is as shown previously (Das et al., 2010).

(B) Structural superposition of TmMre11 with human MRE11, highlighting the inhibitor binding sites. Key amino acid residues are shown in stick representation, with bound manganese ions represented as spheres. The ligands fit into a hydrophobic pocket formed by the dimerization of Mre11, in proximity to the active site. For TmMre11-Mirin-PFM39 (top left hand section) only the binding mode with the aniline moiety orientated towards the active site is shown. The pseudothiohydantoin moiety of mirin is oriented towards the active site displacing the side-chain of His94 from one of its positions in the inhibitor-free structure. His94 is contained within a flexible loop important for endonuclease catalytic activity. The ligand is adjacent to and confined by 2 conserved amino acid motifs in TmMre11 (Gly57-Asp58-Leu59 and Gly92-Asn93-His94-Asp95), which are conserved across all species. TmMre11-Mirin-3T11 imposed (top right hand section) shows superposition of human MRE11 (PDB: 3T1I, coloured cyan) with the co-crystal structure of TmMre11 with mirin. Key amino acids are shown in stick representation and identities labelled in black text for hMRE11 and red for TmMre11. The conserved amino acid motifs found adjacent to mirin bound to TmMre11 are conserved in the human enzyme (Gly59-Asp60-Leu61 and Gly127-Asn128-His129-Asp130). Our structures define these areas as flexible loops that can be influenced by ligand binding. The loop containing the first motif is slightly shifted towards the right in the human enzyme, but would be readily repositioned upon ligand binding. Similarly, His129 of the second motif, is orientated towards the active site in the human structure, but again would be perturbed upon ligand binding.

TmMre11-PFM01-PFM03 (bottom left hand) shows overlay of TmMre11 in complex with either PFM01 or PFM03. The ligands fit into a distinct hydrophobic pocket formed by the dimerization of Mre11, in proximity to the active site. For orientation, the side chain of amino acid Phe102, from both Mre11's domains (labelled A and B) is indicated. Two leucine residues (71 and 78 from helix $\alpha 2$) coordinate one side of the ligand, with the aromatic phenol ring of PFM01 forming a pi-pi stacking arrangement with the side-chain of Trp96. The ligands also partially stack with the side-chain of His94, which is contained within a flexible loop important for endonuclease catalytic activity. The alkyl chain of the ligand, also forms a stacking arrangement with the side-chain of Phe102 from the other domain. TmMre11-PFM01-3T11 (bottom right hand) shows superposition of human MRE11 with the co-crystal structure of tmMre11 with PFM01. The two leucine residues forming part of the ligand binding pocket are conserved in the human enzyme (Leu72 and Leu79 of helix $\alpha 2$). Re-positioning of helix $\alpha 3$, relative to $\alpha 2$ to generate a larger cavity, could accommodate ligand binding in hMRE11.

(C) Dose response of mirin or PFM39 on MRN exonuclease activity. MRN was used at 10 nM concentration and incubated with dsDNA for 30 min. Error bars represent SEM from >3 experiments.

(D) TmMre11 exonuclease assays were performed at 65°C and incubated with dsDNA for 30 min with DNA or inhibitors (0.8 mM). The sequence of dsDNA is shown in the Materials and Methods. TmMre11 exonuclease activity is also inhibited by mirin or PFM39, but not PFM03.

(E) hMRN (400 ng + ATP + Mn) endonuclease activity was examined in the presence of 100 μ M inhibitors. Endonuclease activity of hMRN inhibition is plotted as % circular ssDNA degraded relative to that in the control (DMSO) treated sample. Results represent the mean and standard error (SE) from 3 experiments.

(F) Endonucleolytic cleavage of circular ssDNA phiX174 DNA was assayed with TmMre11 (gene Tm1635 full length) in presence of 5 mM Mre11 inhibitors. PFM03, but not mirin or PFM39, inhibits TmMre11 endonuclease activity. The mutant TmMre11 H94S is used as a negative control since this protein does not display endonuclease activity. 1. DNA ladder; 2. No enzyme; 3. TmMre11 (gene Tm1635 full length) + DMSO; 4. TmMre11 H94S (gene Tm1635) no endonuclease activity (Das et al., 2010); 5. TmMre11 + mirin; 6. TmMre11 + PFM39; 7. TmMre11 + PFM01; 8. TmMre11 + PFM03. Lane 7 (PFM01) did not inhibit endonuclease activity due to lack of solubility *in vitro*.

(G) MRE11 DNA binding is not affected by mirin. 10 nM MRN was added to a ssDNA substrate bound to magnetic beads in the presence or absence of mirin at the indicated concentration. The DNA was then retrieved by pull-down and MRE11 detected using Anti-His antibodies. Left panel shows a diagram of the ssDNA binding assay; the right panel shows the level of MRE11 bound on beads alone or on ssDNA-beads.

(H) MRN DNA binding is examined by an electrophoretic mobility shift (EMSA) assay in the presence of PFM03. Quantification of the results is shown in the right panel. The data represents the mean values from three independent experiments using 10 nM MRN and the indicated concentration of inhibitors.

(I) MRN ATPase assays in the presence of DMSO, mirin, PFM03 or PFM39 at the indicated concentration. ATPase assays were performed as described previously (Bhaskara et al., 2007). Error bars represent SEM from >3 experiments. MRN ATPase activity is mildly reduced by high concentrations of the inhibitors. For the MRN complex, the MRE11 nuclease and RAD50 ATPase activities are believed to be intimately linked (Majka, J. et al, 2012). These assays show a 30~50% ATPase inhibition consistent with the predicted coupled activities of the two inhibitors and the linkage between MRN nuclease and ATPase activities. Estimated IC₅₀ values of inhibitors: For the *in vivo* analysis based on pRPA formation and

chromatin bound RPA assay (Figure S2 and Figure 2B), the IC_{50} is estimated to be 50-75 μM for PFM01, PFM03 and PFM39 and 200-300 μM for mirin. For the exonuclease activity *in vitro*, the IC_{50} for PFM39 inhibition of exonuclease activity is <100 μM ; for mirin ~200 μM (Figure S2A). For the endonuclease activity *in vitro* using MRE11, the IC_{50} for PFM03 is ~100 μM (Figure 1D). Although the *in vitro* and *in vivo* IC_{50} values are within a similar range, differences are likely due to the nature of the *in vivo* substrate, the coupling of endo and exonuclease activities, and the *in vivo* concentration of MRN.

Figure S2

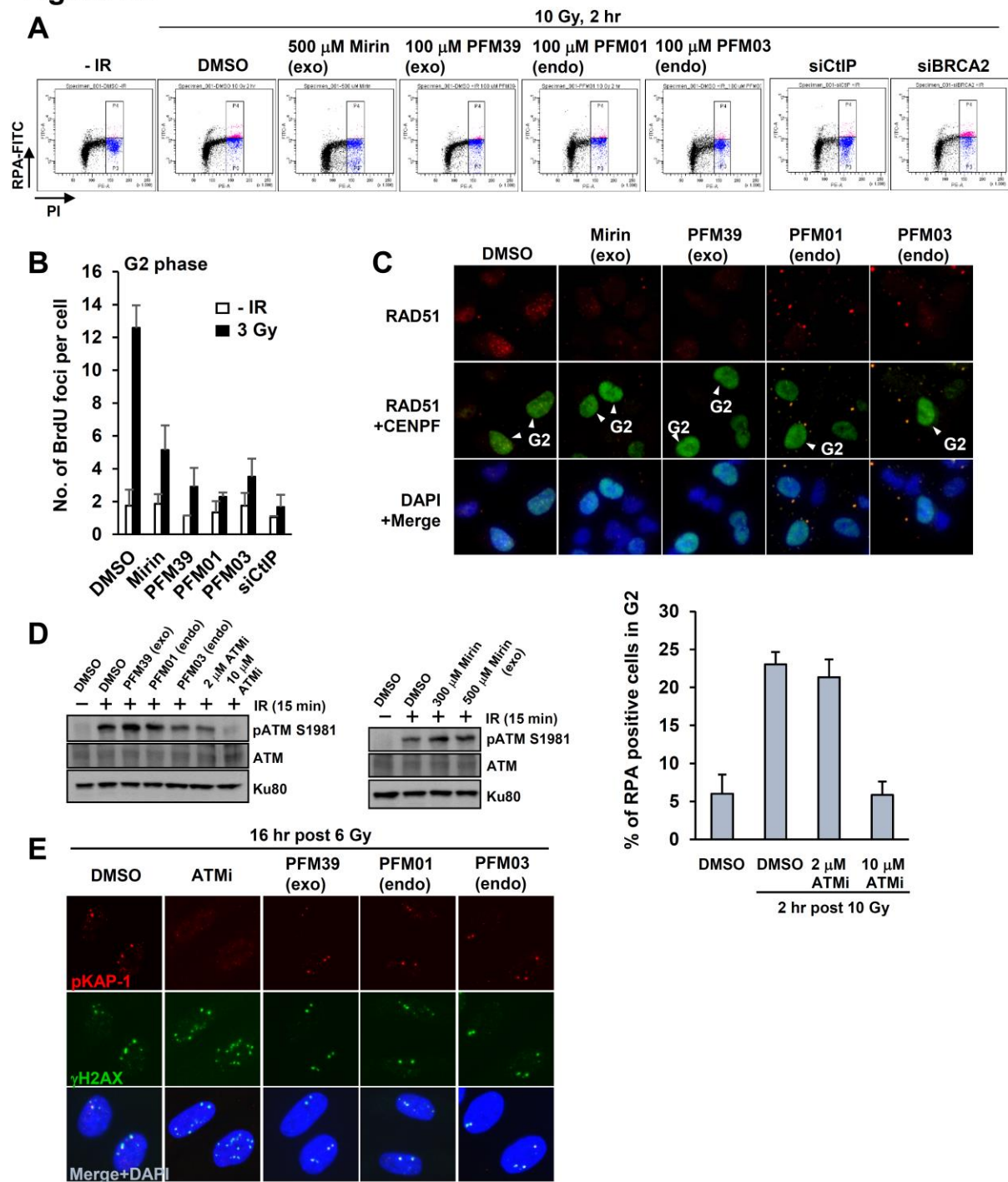


Figure S2, related to Figure 2, shows the analysis of RPA, ssDNA and RAD51 foci and that the inhibitors do not affect ATM activation.

Legend to Figure S2.

(A) The chromatin retention of RPA in G2 cells was analysed using α -RPA antibody after detergent extraction. Chromatin-associated RPA in A549 cells was detected as an Alex488 signal following FACS. G2 cells are detected and gated by PI staining. Quantification of the signal from >3 experiments is shown in Figure 2B.

(B) Analysis of ssDNA levels following inhibitor treatment by monitoring BrdU foci formation. 20 μ M BrdU was added 48 h before 3 Gy IR. Cells were extracted with 0.2% Triton for 1 min at 2 h after IR and stained with a-BrdU antibody without denaturation. Irradiated G2 cells were identified by CENPF. Error bars represent SEM from >3 experiments.

(C) A representative image of IR-induced RAD51 foci formation. Inhibitors were added 30 min before 3 Gy. Irradiated A549 cells were stained with RAD51 and CENPF (G2 marker) following detergent extraction. To prevent irradiated S phase cells progressing into G2, 4 μ M aphidicolin (APH) was added post irradiation in B and C.

(D) MRE11 nuclease activities are dispensable for ATM activation. To examine levels of ATM activation at two ended DSBs and excluding replication coupled breaks in S phase, pATM S1981 in G0/G1 arrested cells was measured by Western Blot analysis. Following 3-5 days after cells reached 100% confluency, ~95% of the cells were confirmed to be in G0/G1 phase by FACS (data not shown). 48BR primary G1 cells were irradiated with 6 Gy +/- inhibitors. The inhibitors did not significantly impede ATM activation. Right panel; PFM03 caused a slightly reduced level of pS1981-ATM, but drug-based inhibition of 2 μ M ATM (KU55933) to achieve a similar level of pATM S1981 did not affect resection monitored by % RPA positive cells after 10 Gy IR. 10 μ M ATM inhibitor was used to fully inhibit ATM activity. Error bars represent SEM from >3 experiments.

(E) Normal IR-induced pKAP-1 foci formation in the presence of MRE11 inhibitors. Since pKAP-1 represents an important ATM substrate for DSB repair, we confirmed efficient ATM activation by monitoring pKAP-1 foci levels. pKAP-1 foci in 48BR (WT) primary fibroblast G0/G1 cells were analysed 16 h post 6 Gy. We have previously shown that pKAP1 foci numbers at 16-24 h post IR are dose dependent and the number of background pKAP-1 foci without IR is <1 , demonstrating that the observed pKAP-1 foci are damage dependent (Noon et al., 2010). These results demonstrate that the MRE11 nuclease activities are dispensable for ATM activation at two-ended DSB sites.

Figure S3

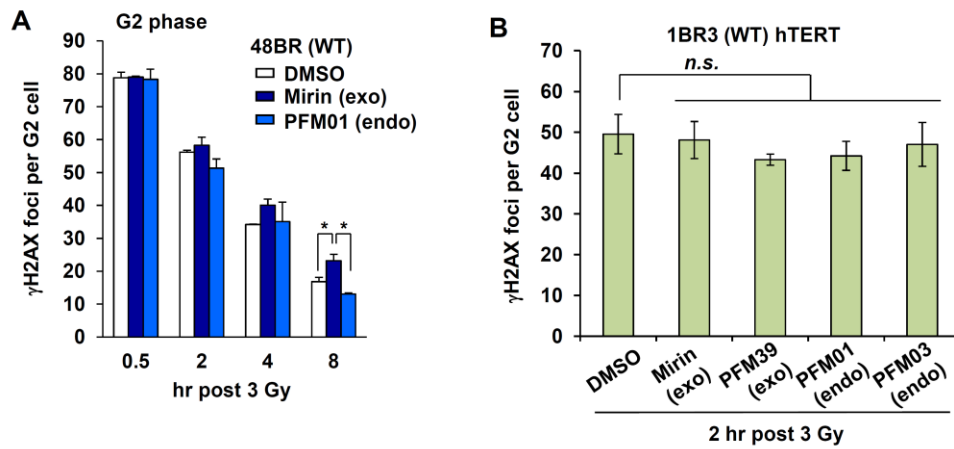


Figure S3, related to Figure 3, shows that MRE11 nuclease is dispensable for NHEJ after ionizing radiation.

(A) A full-time course of γ H2AX analysis post 3 Gy in 48BR (WT) primary fibroblast cells +/- inhibitors is shown. Error bars represent SEM from 3 experiments.

(B) MRE11 nuclease activities are dispensable for core-NHEJ up to 2 h post IR. 1BR3 (WT) hTERT cells were fixed and stained at 2 h post 3 Gy. Error bars represent SEM from 3 experiments. 4 μ M APH was added post irradiation in A and B.

Figure S4

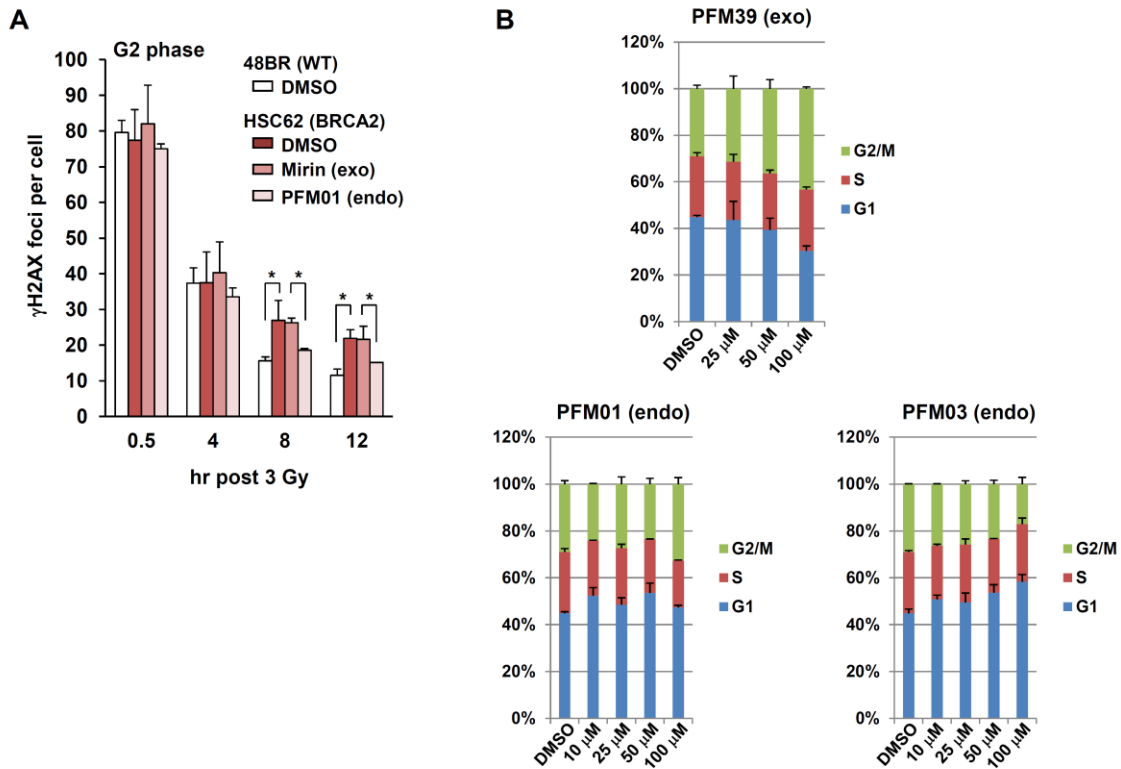


Figure S4, related to Figure 4 shows detailed analysis of DSBs repair in BRCA2 deficient cells.

(A) A full-time course analysis for the impact of MRE11 inhibitors in HSC62 (BRCA2-defective) cells. Results for the 8 h time point are shown in Figure 4A. Whilst no significant difference in DSB repair is detected up to 4 h post 3 Gy, BRCA2- cells exhibit a statistically significant repair defect at 8-12 h post IR. Importantly, the repair defect is alleviated by treatment with MRE11 endonuclease inhibitor. Error bars represent SEM from 3 experiments. 4 μ M APH was added post irradiation.

(B) Cell cycle distribution was analysed by FACS following 24 h incubation in the presence of MRE11 inhibitors at the indicated concentrations. Distribution of each cell cycle is not dramatically affected up to 50 μ M. Therefore, the frequency of HR or NHEJ was analysed with 50 μ M MRE11 inhibitors (see Figures 4E and 5E). Error bars represent SEM from 2 experiments.

Figure S5

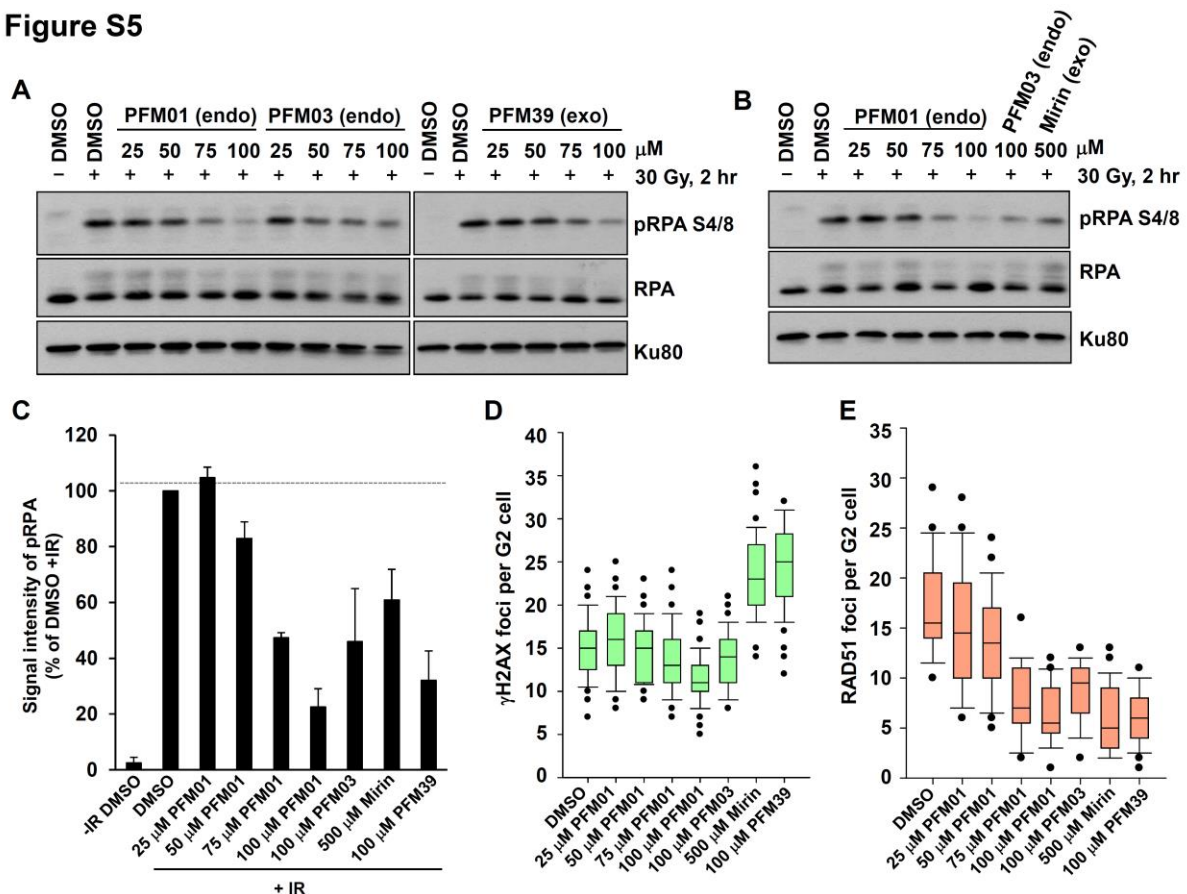


Figure S5, related to Figure 5 shows that pathway choice is determined by specific inhibition of MRE11 endonuclease activity.

(A-C) Since we reproducibly observed that the level of residual RPA phosphorylation by Western Blotting (which is a more sensitive assay than examining chromatin-bound RPA by FACS analysis) was greater in exonuclease versus endonuclease-inhibitor treated cells following IR, we examined whether the magnitude of resection determines DSB repair pathway choice rather than the specificity of MRE11 endo versus exo-nuclease activity. To verify that specific inhibition of MRE11 endonuclease activity confers a DSB repair defect, we titrated the inhibitor concentrations. The levels of IR-induced pRPA S4/8 were examined in A549 cells 2 h post 30 Gy. The titration revealed that 75 μ M PFM01 inhibits resection to a comparable level to that of 500 μ M mirin or 100 μ M PFM39 (the concentration routinely used to inhibit the exonuclease activity). Quantification of pRPA signal normalised to Ku80

from two independent experiments is shown in (C). Error bars represent SEM from 2 experiments.

(C-E) However importantly, 75 μ M PFM01 does not confer a DSB repair defect in contrast to the defect observed using the exonuclease inhibitors. Consistent with the impact on resection, both inhibitors abolish RAD51 foci formation at these concentrations. γ H2AX analysis and RAD51 foci formation were performed in 1BR3 (WT) hTERT at 8 or 2 h post 3 Gy, respectively. Thus, we conclude that DSB repair pathway choice is determined by the specific inhibition of MRE11 endo-nuclease activity rather than it being a consequence of the magnitude of resection at DSB sites. 4 μ M APH was added post irradiation in D and E.

Figure S6

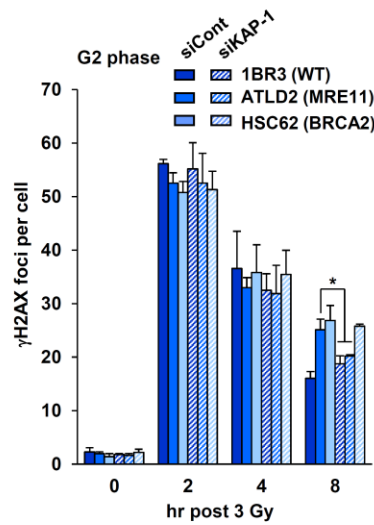


Figure S6 related to Figure 6 shows that KAP1 siRNA alleviates the DSB repair defect in ATLD2 cells.

Depletion of KAP-1 alleviates the DSB repair defect in ATLD2 cells, but not HSC62 cells.

The result suggests that the repair defect in ATLD2 cells is caused by impaired chromatin modification. DSB repair in G2 cells are examined by γ H2AX foci analysis post 3 Gy. Error bars represent SEM from >3 experiments. 4 μ M APH was added post irradiation.

Figure S7

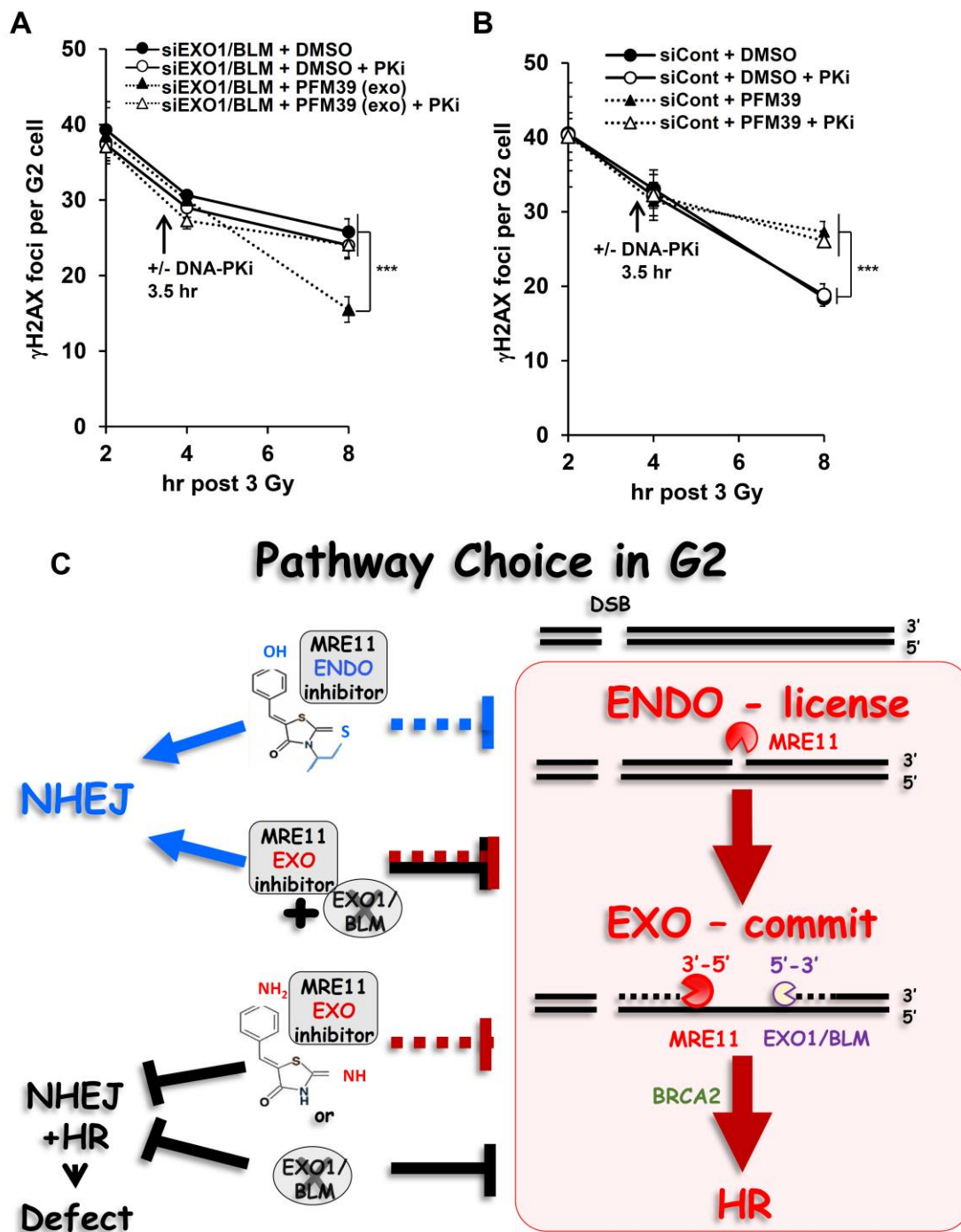


Figure S7, related to Figure 7 shows that MRE11 exonuclease inhibitor and knockdown of EXOI block HR and presents a figure summarizing the findings.

Legend to Figure S7.

(A) Following addition of MRE11 exo-inhibitor and EXO1/BLM siRNA DSB repair switches from HR to NHEJ. The addition of the DNA-PKi prevents DSB repair following combined loss of the two exonucleases demonstrating that DSBs are repaired by NHEJ instead of HR. Error bars represent SEM from >3 experiments.

(B) NHEJ usage in the presence of MRE11 inhibitors was examined by adding a DNA-PK inhibitor (DNA-PKi) at 3.5 h post 3 Gy. We have previously demonstrated that the fast component of DSB repair requires core NHEJ, and that the majority of NHEJ is completed by 4 h post 3 Gy. Thus, addition of the DNA-PKi at 3.5 h does not affect DSB repair kinetics in control cells, since the remaining DSBs undergo repair by HR. Following 3 Gy, DSB repair in A549 cells + siControl was examined by γ H2AX foci analysis +/- PFM39 +/- DNA-PKi (post-treatment). Importantly, the addition of the DNA-PKi in siControl + PFM39 cells does not affect DSB repair from 4 to 8 h, demonstrating that the repair defect is solely due to lack of HR repair. 4 μ M APH was added post irradiation. Error bars represent SEM from >3 experiments.

(C) Cartoon summarising the impact of MRE11 nuclease inhibitor on DSB repair pathway choice.

Table S1. X-Ray Diffraction Data Collection and Refinement Statistics
(Molecular Replacement)

	TmMre11-Mirin	TmMre11-PFM39	TmMre11-PFM01	TmMre11-PFM03	TmMre11 WT APO
Data					
Space group	P 1 2 1 1	P 1 2 1 1	P 1 2 1 1	P 1 2 1 1	P 1 2 1 1
Cell					
<i>a</i> , <i>b</i> , <i>c</i> (Å)	47.77, 113.15, 80.89	47.72, 113.42, 80.48	48.18, 113.53, 81.56	48.06, 113.94, 81.57	47.12, 109.95, 76.92
α, β, γ (°)	90, 101.47, 90	90, 101.28, 90	90, 101.28, 90	90, 100.31, 90	90, 100.21, 90
Resolution (Å)	50.0-2.1 (2.18- 2.10)*	50.0-2.3 (2.38- 2.30)	50.0-2.3 (2.38- 2.30)	50.0-2.4 (2.49- 2.40)	50.0-1.9 (1.97-1.9)
<i>R</i> _{sym} or <i>R</i> _{merge}	4.3 (30.3)	5.1 (60.5)	4.2 (29.2)	5.3 (65.7)	7.8 (62.1)
<i>I</i> / σ	39.4 (2.89)	33.2 (2.3)	41.6 (6.9)	24.2 (1.7)	28.7 (2.4)
Completeness	94.5 (66.5)	99.7 (98.7)	94.8 (99.6)	94.8 (98.3)	99.7 (100.0)
Redundancy	3.4 (2.1)	3.7 (3.3)	3.5 (3.5)	3.7 (3.5)	3.6 (3.6)
Refinement					
Resolution (Å)	50.0-2.1	50.0-2.3	50.0-2.3	50.0-2.4	50.0-1.9
No.	43542	37056	34034	24749	54461
Reflections/Ob					
<i>R</i> _{work} / <i>R</i> _{free}	19.4/24.2	19.2/23.0	20.0/25.9	19.4/25.6	23.1/26.5
No. atoms	5322	5324	5288	5321	5534
Protein	5157	5153	5143	5157	5225
Ligand/ion	4 (Mn) 30 (Mirin)	4 (Mn) 30 (PFM39)	4 (Mn) 38 (PFM01)	4 (Mn) 38 (PFM03)	4 (Mn)
Waters	131	137	103	122	305
B-factors					
Protein	53.8	54.9	48.2	53.7	52.3
Ligand/ion	134.5	135.7	66.6	72.5	36.0
Water	47.9	44.5	40.2	41.9	51.0
R.m.s.					
Bond	0.008	0.004	0.003	0.004	0.004
Bond	1.240	0.845	0.878	0.809	0.890

*1 crystal was used for each structure. *Values in parentheses are for highest-resolution shell.

Supplemental Experimental Procedures

Antibodies

γ H2AX (05-636 (JBW301); Upstate Biotechnology, Buckingham, UK for IF and EP854(2)Y; Epitomics for laser experiment), CENPF (ab5; Abcam, Cambridge, UK), RPA (NA-18, Ab-2; Calbiochem for IF and FACS, LS-C38952; LifeSpan BioSciences for WB), pRPA S4/8 (A300-245A, Bethyl Laboratories), RAD51 (sc-8349 (H-92); Santa Cruz, Santa Cruz, CA), Ku80 (2180 (C48E7); Cell Signaling), BRCA2 (OP95; Calbiochem), pKAP-1 S824 (A300-767A; Bethyl Laboratories), KAP-1 (ab3831; Abcam, Cambridge, UK), MRE11 (12D7, GTX70212; GeneTex, USA for laser experiment), NBS1 (PC269, Ab-1; Oncogene), RAD50 (3427; Cell Signaling), pATM S1981(2152-1; Epitomics), ATM (GTX70103 (2C1); GeneTex), pChk2 T68 (2661; Cell Signaling), Chk2 (ab8108; Abcam, Cambridge, UK), 53BP1 (A300-272A; Bethyl Laboratories) and β -tubulin (ab21058; Abcam, Cambridge, UK).

General procedure for the one-pot synthesis of (Z)-3-alkyl-5-(4-hydroxybenzylidene)-2-thioxothiazolidin-4-one derivatives

Bis(carboxymethyl)trithiocarbonate (113 mg, 0.5 mmol) was dissolved in DME (1 mL). TEA (70 μ L, 0.5 mmol) and the proper amine (0.5 mmol) were added and the reaction mixture irradiated with microwaves at 90 °C for 10 minutes, 2 times. 4-OH-benzhaldehyde (61 mg, 0.5 mmol) was then added and the suspension obtained irradiated with microwaves at 110 °C for 10 minutes, 2 times. The solution was evaporated under reduced pressure and purified by flash chromatography (eluent AcOEt/PE: from 1:3 to 1:0) giving the expected product.

(Z)-3-iso-butyl-5-(4-hydroxybenzylidene)-2-thioxothiazolidin-4-one (PFM01):

Yellow solid (51 mg, 0.17 mMol, yield 30%). ¹H-NMR (400 MHz, CDCl₃, 323 K, δ ppm, J Hz) 7.64 (s, 1H); 7.38 (d, J = 8.4 Hz, 2H); 6.93 (d, J = 8.4 Hz, 2H); 6.02 (bs, 1H); 3.94 (d, J = 7.2 Hz, 2H); 2.35-2.28 (m, 1H); 0.92 (d, J = 6.4 Hz, 6H). ¹³C-NMR (100 MHz, CDCl₃, 323 K, δ ppm, J Hz) 168.6; 158.1; 133.1; 126.2; 119.9; 116.5; 114.7; 51.5; 26.8; 20.0. ES/MS: m/z 292 [M-1]-

(Z)-3-sec-butyl-5-(4-hydroxybenzylidene)-2-thioxothiazolidin-4-one (PFM03):

Yellow solid (83 mg, 0.28 mMol, yield 55%). ¹H-NMR (200 MHz, CDCl₃, 323 K, δ ppm, J Hz) δ 7.55 (s, 1H); 7.35 (d, J = 8 Hz, 2H); 6.93 (d, J = 8 Hz, 2H); 6.18 (bs, 1H) 5.27-5.11 (m, 1H); 1.92-1.78 (m, 2H); 1.49 (d, J = 6 Hz, 3H); 0.86 (t, J = 8 Hz, 3H). ¹³C-NMR (50 MHz, CDCl₃, 323 K, δ ppm, J Hz) 168.6; 158.1; 133.1; 126.2; 119.9; 116.5; 114.7; 52.3; 26.8; 20.0; 15.9. ES/MS: m/z 292 [M-1]-

Synthesis of (Z)-2-Imino-5-(4-nitrobenzylidene)thiazolidin-4-one:

To a stirred suspension of 4-nitrobenzaldehyde (1 g, 6.6 mmol) and 2-iminothiazolidin-4-one (0.64 g, 5.5 mmol) in glacial AcOH (25 mL) NaOAc was added (1.06 g, 12.9 mmol) and the reaction mixture refluxed for 4 h. The reaction mixture was then cooled to 4 °C and the solid obtained filtered over Büchner and washed with H₂O (3 x 10 mL) and dried giving 1.3 of an orange solid (95% yield).

¹H-NMR (400 MHz, DMSO, 323 K, δ ppm, JHz) δ 9.37 (bs, 1H); 8.74 (bs, 1H); 7.55 (d, J = 8.4 Hz, 2H); 6.97 (d, J = 8.4 Hz, 2H); 6.83 (s, 1H). ¹³C-NMR (100 MHz, DMSO, 323 K, δ ppm, JHz) δ 175.2 (C=O), 169.5 (C=NH), 147.0 (C-NO₂), 140.8, 134.1, 130.3, 126.3, 124.3 ES/MS: m/z 250 [M+1]+

Synthesis of (Z)-2-Imino-5-(4-aminobenzylidene)thiazolidin-4-one (PFM39):

To a solution of (Z)-2-Imino-5-(4-nitrobenzylidene)thiazolidin-4-one (200 mg, 0,8 mmol) in EtOH (15 ml), SnCl₂ (900 mg, 4,2 mmol) was added and the reaction mixture refluxed for 1 hour. The solution was filtered over Büchner. The EtOH solution was dried and an orange solid obtained and purified by flash chromatography (gradient elution: CH₂Cl₂/MeOH from 1:0 to 9:1). 84 of an orange solid were obtained (48% yield).

¹H-NMR (400 MHz, CD₃OD, 323 K, δ ppm, JHz) δ 7.81 (s, 1H); 7.12 (d, J = 8.4, 2H); 7.05 (d, J=8, 2H); 5.21(bs, 2H). ES/MS: m/z 220 [M+1]⁺

Supplemental References

Bhaskara V, Dupré A, Lengsfeld B, Hopkins BB, Chan A, Lee JH, Zhang X, Gautier J, Zakian V, Paull TT. (2007). Rad50 adenylate kinase activity regulates DNA tethering by Mre11/Rad50 complexes, *Mol. Cell*, 25, 647-661.

Das, D., Moiani, D., Axelrod, H.L., Miller, M.D., McMullan, D., Jin, K.K., Abdubek, P., Astakhova, T., Burra, P., Carlton, D., *et al.* (2010). Crystal structure of the first eubacterial Mre11 nuclease reveals novel features that may discriminate substrates during DNA repair. *J. Mol. Biol.* 397, 647-663.

Majka J, Alford B, Ausio J, Finn RM, McMurray CT. (2012). ATP hydrolysis by RAD50 protein switches MRE11 enzyme from endonuclease to exonuclease. *J. Biol. Chem.*, 287, 2328-2341.

Noon, A.T., Shibata, A., Rief, N., Lobrich, M., Stewart, G.S., Jeggo, P.A., and Goodarzi, A.A. (2010). 53BP1-dependent robust localized KAP-1 phosphorylation is essential for heterochromatic DNA double-strand break repair. *Nat. Cell Biol.* 12, 177-184.